# Analysis of $\beta_2$AR-$G_s$ and $\beta_2$AR-$G_i$ complex formation by NMR spectroscopy

Xiuyan Ma[a], Yunfei Hu[b,c], Hossein Batebi[d], Jie Heng[a], Jun Xu[a], Xiangyu Liu[a,e], Xiaogang Niu[b], Hongwei Li[b], Peter W. Hildebrand[d,f,g], Changwen Jin[b,1], and Brian K. Kobilka[a,h,1]

[a]Beijing Advanced Innovation Center for Structural Biology, School of Medicine, Tsinghua University, Beijing 100084, China; [b]Beijing Nuclear Magnetic Resonance Center, College of Chemistry and Molecular Engineering, Peking University, Beijing 100084, China; [c]Innovation Academy for Precision Measurement Science and Technology, Chinese Academy of Science, Wuhan, 430071, China; [d]Institute of Medical Physics and Biophysics, University Leipzig, 04107 Leipzig, Germany; [e]School of Pharmaceutical Sciences, Tsinghua University, Beijing 100084, China; [f]Institute of Medical Physics and Biophysics, Charité Medical University Berlin, Berlin, Germany; [g]Berlin Institute of Health, 10178 Berlin, Germany; and [h]Department of Molecular and Cellular Physiology, Stanford University School of Medicine, Stanford, CA 94305

The $\beta_2$-adrenergic receptor ($\beta_2$AR) is a prototypical G protein-coupled receptor (GPCR) that preferentially couples to the stimulatory G protein $G_s$ and stimulates cAMP formation. Functional studies have shown that the $\beta_2$AR also couples to inhibitory G protein $G_i$, activation of which inhibits cAMP formation [R. P. Xiao, Sci. STKE 2001, re15 (2001)]. A crystal structure of the $\beta_2$AR-$G_s$ complex revealed the interaction interface of $\beta_2$AR-$G_s$ and structural changes upon complex formation [S. G. Rasmussen et al., Nature 477, 549–555 (2011)], yet, the dynamic process of the $\beta_2$AR signaling through $G_s$ and its preferential coupling to $G_s$ over $G_i$ is still not fully understood. Here, we utilize solution nuclear magnetic resonance (NMR) spectroscopy and supporting molecular dynamics (MD) simulations to monitor the conformational changes in the G protein coupling interface of the $\beta_2$AR in response to the full agonist BI-167107 and $G_s$ and $G_{i1}$. These results show that BI-167107 stabilizes conformational changes in four transmembrane segments (TM4, TM5, TM6, and TM7) prior to coupling to a G protein, and that the agonist-bound receptor conformation is different from the G protein coupled state. While most of the conformational changes observed in the $\beta_2$AR are qualitatively the same for $G_s$ and $G_{i1}$, we detected distinct differences between the $\beta_2$AR-$G_s$ and the $\beta_2$AR-$G_{i1}$ complex in intracellular loop 2 (ICL2). Interactions with ICL2 are essential for activation of $G_s$. These differences between the $\beta_2$AR-$G_s$ and $\beta_2$AR-$G_{i1}$ complexes in ICL2 may be key determinants for G protein coupling selectivity.

GPCR | $\beta_2$-adrenergic receptor | NMR spectroscopy | G protein coupling specificity

G protein-coupled receptors (GPCRs) are the largest family of membrane proteins responsible for most of the transmembrane signal transduction processes. The activation of GPCRs is mediated by diverse stimuli, including neurotransmitters, hormones, ions, and photons. It is now well known that GPCRs can activate different signaling pathways through coupling with distinct downstream transducers, for example G proteins and arrestins (1). It is generally accepted that GPCRs are highly dynamic proteins that can adopt multiple distinct conformations depending on the ligands, lipids, environments, and signaling transducers through a conformational selection mechanism (1, 2). The $\beta_2$ adrenergic receptor ($\beta_2$AR) has been an important model system for studying aspects of GPCR biology and pharmacology for more than 40 y. The $\beta_2$AR can activate more than one G protein isoform. While preferentially coupling to the stimulatory G protein ($G_s$), which activates adenylyl cyclase, it also couples to the inhibitory G protein family ($G_{i/o}$) (3), which inhibits adenylyl cyclase (Fig. 1A).

The structure of the $\beta_2$AR-$G_s$ complex revealed the interaction between $\beta_2$AR and $G_s$, and the structural changes that take place upon complex formation (4), yet, the dynamic process of $\beta_2$AR signaling through $G_s$ is still not fully understood. The structural features of the $\beta_2$AR-$G_s$ complex have been observed in GPCR-G protein complexes for $G_i$, $G_o$, and $G_{11}$ proteins determined by cryo-electron microscopy (cryo-EM) (5–7); however, the molecular mechanism of G protein coupling specificity is still unclear. This may in part be due to the fact that all of the GPCR-G protein complex structures solved so far are captured in a biochemically stable nucleotide-free state, while specificity determination may happen at an earlier stage of complex formation. Single-molecule studies of the $\beta_2$AR coupling to $G_s$ provide evidence for at least one intermediate state (8). The existence of intermediate states is further supported by monitoring $\beta_2$AR-$G_s$ complex formation using time-resolved radiolytic footprinting and hydrogen-deuterium exchange (9).

NMR spectroscopy has previously been used to study GPCR dynamics (10–16). Several site-specific isotopic labeling strategies have been shown to be feasible for studying conformational dynamics of GPCRs, such as $^{13}$C-dimethylated lysine, $^{13}$CH$_3$-ε-methionine, and $^{19}$F-labeled cysteine (17). Previous NMR studies of the $\beta_2$AR using these methods have revealed weak allosteric coupling between ligand binding domain and G protein coupling domain, and that the $\beta_2$AR can adopt multiple conformational states during activation (11–13). However, due to the limitation of large molecular weight and difficulty in sample preparation, little is

## Significance

Recent structures of GPCRs in complex with G proteins provide important insights into G protein activation by family A and family B GPCRs; however, important questions remain. We don't fully understand the mechanism of G protein coupling specificity or coupling promiscuity of some GPCRs. The $\beta_2$AR preferentially couples to $G_s$ and less efficiently to $G_i$, yet $\beta_2$AR-$G_i$ coupling has been shown to play important roles in cardiac physiology. To better understand the structural basis for the preferential coupling of the $\beta_2$AR to $G_s$ over $G_i$, we used NMR spectroscopy and supporting MD simulations to study the conformational changes in the intracellular surface of the $\beta_2$AR. These studies reveal a distinct difference in intracellular loop 2 interactions with $G_s$ and $G_{i1}$.
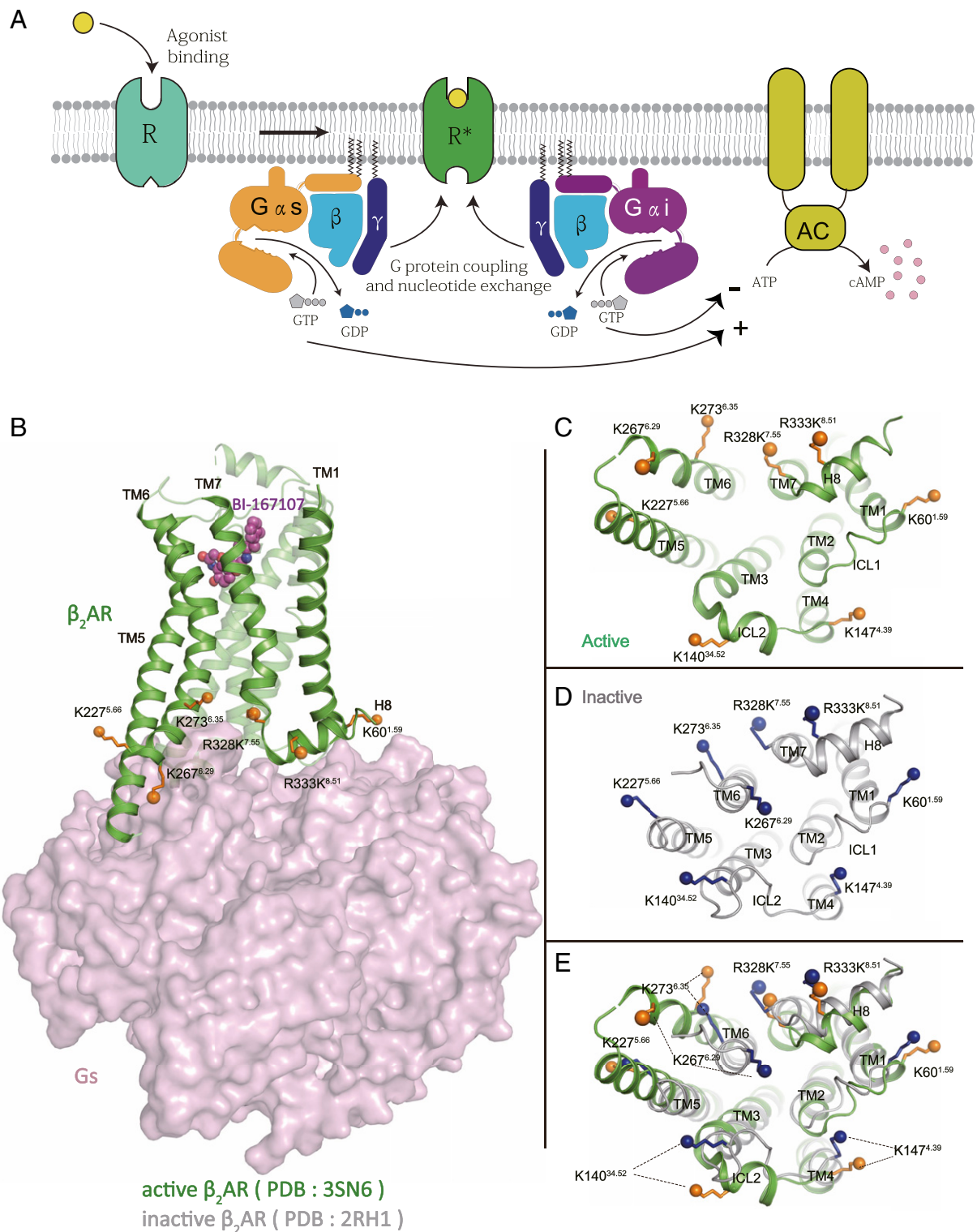
**Fig. 1.** The β₂AR-G protein signaling pathways. (*A*) The agonist-bound β₂AR activates either G$_s$ or G$_i$ heterotrimer, which stimulates or inhibits the adenylyl cyclase activity, respectively. (*B*) Structure of β₂AR-Gs complex (PDB ID code: 3SN6), the lysine residues that are chosen as NMR probes are shown as solid spheres, other lysine residues were mutated to arginine as described in the text. (*C–E*) The lysine probes undergo conformational changes during the activation of the β₂AR, as shown by cytoplasmic views of active β₂AR (PDB ID code: 3SN6) (*C*), inactive β₂AR (PDB ID code: 2RH1) (*D*), and the overlap of active and inactive β₂AR (*E*).

known about the conformational dynamics of the β₂AR in response to different G protein subtypes. In this study, we utilized ¹³C-dimethylated lysine as an NMR probe to investigate the conformational changes of several sites in the intracellular G protein

binding interface of the β₂AR. ¹³C-dimethylated lysine is an ideal probe for this purpose because of its large, flexible side chain, enabling studies of larger protein complexes. Our studies show that in addition to TM6, agonist binding can also promote

Ma et al.

conformational changes in TM4, TM5, and TM7. We observe further structural changes in $\beta_2$AR coupled to $G_s$ and $G_{i1}$. While the structural changes stabilized by $G_s$ and $G_{i1}$ are qualitatively similar in most cytoplasmic domains probed, we detected distinct differences between the $\beta_2$AR-$G_s$ and the $\beta_2$AR-$G_{i1}$ complex in intracellular loop 2 (ICL2). In the inactive-state structure of the $\beta_2$AR, ICL2 is a loop, while in the $\beta_2$AR-$G_s$ complex, ICL2 forms an $\alpha$-helix that positions F139[34.51] in ICL2 to engage a hydrophobic pocket in $G_{\alpha s}$, thereby triggering nucleotide release (4).

## Results

### Design of Modified $\beta_2$ARs for $^{13}$C-Dimethylated Lysine NMR Studies.
$^{13}$C-dimethylated lysine probes have long served as excellent probes for NMR experiments due to high sensitivity and relatively long transverse relaxation times (18). The WT $\beta_2$AR contains 16 lysine residues, most of which are located at the G protein coupling interface (Fig. 1 *B–E* and *SI Appendix*, Fig. S1A). Therefore, these lysine residues can be used as NMR reporters to monitor structural changes in response to agonists and G proteins.

However, previous studies have shown that the $^{13}$C-dimethylated lysine spectra of C-terminally truncated WT $\beta_2$AR ($\beta_2$AR-365N) was too crowded to make assignments (11), probably due to the similar chemical environments of these intracellular lysines. To avoid the NMR signals overlapping, we made a truncated lysine-free $\beta_2$AR construct ($\beta_2$AR-365N-zero-K) by mutating all lysines to arginines as previously reported (19) and removing the C-terminal 48 residues (*SI Appendix*, Fig. S1 *A and D*). Radioligand binding studies show that these modifications have only small effects on the affinity of antagonists and agonists (*SI Appendix*, Fig. S1C). A previous study showed that the lysine-free $\beta_2$AR has functional properties that are comparable to WT $\beta_2$AR in stimulation of adenylyl cyclase activity (19) and the recruitment of $\beta$-arrestin (20). The only reported effect of removing lysine is loss of ubiquitination and subsequent targeting receptor to lysosome for degradation (20). We then individually introduced eight lysines to different transmembrane segments in the intracellular domain of the $\beta_2$AR based on the lysine-free construct (Fig. 1 *B–E* and *SI Appendix*, Fig. S1A). These eight residues were K60[1.59], K140[34.52], K147[4.39], K227[5.56], K267[6.29], K273[6.35], R328K[7.55], R333K[8.51] (superscripts are Ballesteros and Weinstein numbering; ref. 21), located at the intracellular end of TM1, TM4, TM5, TM6, TM7, ICL2, and H8. The resulting eight constructs were expressed, purified, and labeled through reductive methylation (*SI Appendix*, Figs. S1B and S2A). Methylation efficiency was high, as determined by loss of labeling with fluorescamine, an amine reactive fluorophore (*SI Appendix*, Fig. S1B). We applied $^1$H-$^{13}$C heteronuclear single quantum coherence spectroscopy ($^1$H-$^{13}$C HSQC) to each construct. The signal of each lysine was found at around 2.85 ppm in the $^1$H dimension and 45 ppm in the $^{13}$C dimension as compared to the spectrum of lysine-free $\beta_2$AR (*SI Appendix*, Fig. S3 *A–H*). The signals are unlikely from the N terminus because the N-terminal Flag tag was removed after methylation. In order to make sure they are not residual N terminus signals due to incomplete protein digestion, we measured the signals from the methylated N terminus and they are in different positions from the lysine signals (*SI Appendix*, Fig. S3I). For each $\beta_2$AR-365N-one-K construct, we obtained the $^1$H-$^{13}$C HSQC spectra under the following conditions: unliganded (apo-state) $\beta_2$AR, BI-167107-bound, carazolol-bound, BI-167107-bound $\beta_2$AR in complex with Gs or Gi1 in the presence of 300 μM GDP ($G_s^{GDP}$ or $G_{i1}^{GDP}$), and BI-167107-bound $\beta_2$AR in complex with nucleotide-free Gs or Gi1 ($G_s^{EMPTY}$ or $G_{i1}^{EMPTY}$). For these studies we used saturating concentrations of BI-167107, a potent full agonist with a dissociation half-life of 400 min and an association half-life of less than 4.4 min (12). For inverse agonist, we used a saturating concentration of carazolol. The very slow dissociation half-lives for these ligands ensures that they are bound throughout the NMR experiment.

There are crystal structures of carazolol-bound $\beta_2$AR (22) and the BI-167107–bound $\beta_2$AR-$G_s$ complex (4); however, it has not been possible to crystalize native $\beta_2$AR in the apo-state or bound to agonist alone, most likely due to the inherent instability of the receptor under these conditions. While $\beta_2$AR also couples to $G_i$, there are no reported structures of a $\beta_2$AR-$G_i$ complex. Therefore, the NMR experiments provide structural insights into the apo-state, the agonist-bound $\beta_2$AR, and the $\beta_2$AR-$G_{i1}$ complex relative to available crystal structures. Figs. 2–4 show the comparison of $^1$H-$^{13}$C HSQC spectra of the eight $^{13}$C-dimethylated lysine probes in TM1, ICL2, TM4, TM5, TM6, TM7, and Helix-8 in four different conditions: apo-state, inverse agonist-bound, agonist-bound, and agonist + $G_s^{EMPTY}$.

### Apo-$\beta_2$AR Compared to Inverse Agonist-Bound States.
The $\beta_2$AR exhibits basal activity for $G_s$ activation in the apo-state. This activity can be suppressed by inverse agonists such as carazolol. Previous $^{13}$C-methionine and $^{19}$F NMR studies revealed relatively subtle conformational changes when comparing inverse-agonist stabilized inactive-state and the apo-state $\beta_2$AR (12, 13). Consistent with these findings, our results show relatively small spectral changes in several domains of the intracellular surface in apo-state and the carazolol-stabilized inactive state. We observe the largest difference between the apo-state and carazolol-bound inactive state is in K60[1.59] (Fig. 2A), suggesting a change in its chemical environment possibly due to a change in polar interactions with the end of Helix 8 (Fig. 2 *C–F*). In the apo-state, K60[1.59] is represented by strong Peak 1 with a weak shoulder Peak 2. In carazolol-bound receptor we observe an up-field shift in Peak 1 and no change in Peak 2.

In the apo-state we observe two peaks for K147[4.39] at the end of TM4 (Fig. 3), K273[6.35] in TM6, and R328K[7.55] in TM7 (Fig. 4). This suggests the existence of conformational heterogeneity in these receptor domains with exchange between two states on slow time scale (seconds or slower). In K273[6.35] and R328K[7.55] we observe very small up-field shifts in the position of Peak 1 in carazolol-bound receptor compared to the apo-state that are in the opposite direction observed for agonist (Fig. 4 *C and D*).

### Conformational Changes following Agonist Binding and $G_s$ Coupling.
To correlate structural changes observed by NMR with the $\beta_2$AR-$G_s$ crystal structure, we obtained spectra of the $\beta_2$AR bound to nucleotide-free Gs ($\beta_2$AR-$G_s^{EMPTY}$). $\beta_2$AR-$G_s^{EMPTY}$ was formed by adding the nucleotidase apyrase after complex formation to degrade any released GDP. In the $\beta_2$AR-$G_s^{EMPTY}$ crystal structure, the largest structural changes are the outward movement of TM5 and TM6 and inward movement of TM7, which allows the insertion of the $\alpha 5$ helix of $G_{\alpha s}$ (Fig. 1 *C–E* and *SI Appendix*, Fig. S4). We observed obvious spectral changes when comparing $\beta_2$AR bound to agonist alone with the $\beta_2$AR-$G_s^{EMPTY}$ complex in all probes except K333[8.51] in Helix 8 (Figs. 2–4). This may be due to a combined effect of direct $G_s$ protein binding, as well as a fully active conformation stabilized only by agonist and $G_s$ protein, but not agonist alone (13).

*ICL1 and helix 8.* The spectrum of K60[1.59] at the end of TM1 is nearly identical for apo-state and agonist-bound state (Fig. 2A), suggesting little perturbation of conformational dynamics in the junction of TM1 and ICL1. ICL1 and Helix 8 have no direct interaction with $G_s$ in the $\beta_2$AR-$G_s^{EMPTY}$ complex. The observation of intensity reduction upon coupling with $G_s$ for K60[1.59] (Fig. 2A) and K333[8.51] (Fig. 2B) may result from the slower tumbling due to the formation of complex with a much larger molecular weight. We do observe a change in the spectra of K60[1.59] upon coupling to $G_s$. In the inactive state K60[1.59] forms a polar interaction with E338[8.56] in Helix 8 (Fig. 2 *E and F*). This is lost in the $\beta_2$AR-$G_s^{EMPTY}$ complex due to a small ~1.5 Å movement of
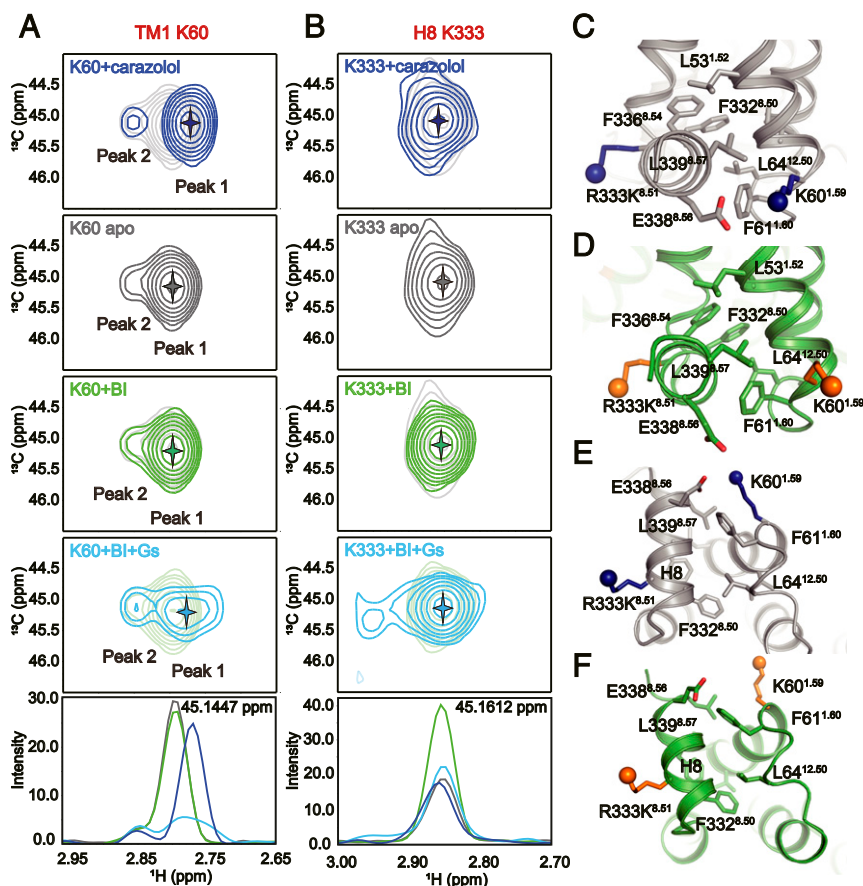
www.manaraa.com

**Fig. 2.** Conformational changes of TM1 and H8 during β$_2$AR activation. (*A* and *B*) The $^1$H-$^{13}$C HSQC spectra of K60$^{1.59}$ from TM1 (*A*) and K333$^{8.51}$ from H8 (*B*). The one-dimensional (1D) slices of corresponding $^1$H-$^{13}$C HSQC spectra in H dimension are shown at the bottom. (*C–E*) The local environments of the two probes are shown by side views in inactive (gray, *C*) and active conformations (green, *D*), as well as cytoplasmic views in inactive (gray, *E*) or active conformations (green, *F*). The agonist BI-167107 is abbreviated by BI.

TM1 away from Helix 8 (Fig. 2 *C* and *D*). We also observe the appearance of a weak downfield peak in R333K$^{8.51}$ in H8.

***ICL2.*** In the inactive state structure of the β$_2$AR, ICL2 has no secondary structure while it is an alpha-helix in the β$_2$AR-G$_s$$^{EMPTY}$ complex (Fig. 3 *C* and *D*). The helix positions F139$^{34.51}$ in ICL2 to engage a hydrophobic pocket formed by H41, V217, F376, C379, R380, and I383 in the G$_{αs}$ subunit (Fig. 3*D*). This interaction is essential for G$_s$ activation (4, 23, 24). The conformational changes detected in the NMR spectra of K147$^{4.39}$ and K140$^{34.52}$ may represent the chemical environment change during the transition of ICL2 from a loop to a helix (Fig. 3 *A* and *B*).

K147$^{4.39}$ is located at the junction of TM4 and ICL2 (Fig. 1 *C* and *D*). In the inactive state, K147$^{4.39}$ forms a hydrogen bond with the backbone carbonyl of Q65$^{12.51}$ in ICL1 (Fig. 3*E*). This interaction is lost in the structure of β$_2$AR-G$_s$$^{EMPTY}$ (Fig. 3*F*). In the apo state, the two peaks likely represent an equilibrium between the formation (Peak 2) and disruption (Peak 1) of the hydrogen bond in slow exchange (Fig. 3*B*). The observation of one dominant peak for K147$^{4.39}$ in the agonist-bound state compared to the two peaks in the apo-state most likely suggests faster exchange rate between the different conformations observed in the apo state (Fig. 3*B*). In β$_2$AR-G$_s$ complex we observe predominantly Peak 1, consistent with the loss of the hydrogen bond (Fig. 3*B*).

In contrast to the dynamics in the junction of TM4 and ICL2 observed in the apo and agonist-bound receptor, we observe a strong single peak for K140$^{34.52}$ at the junction of ICL2 and TM3 (Fig. 3*A*). In the inactive state, K140$^{34.52}$ forms a hydrogen bond

with Q229$^{5.58}$ in TM5, while in the β$_2$AR-G$_s$ complex it is adjacent to the β$_2$AR-G$_s$ interface (Fig. 3 *C* and *D*). Coupling with G$_s$ dramatically alters the chemical environment of K140$^{34.52}$, as evidenced by the appearance of a new downfield peak (labeled as peak2). Only a small fraction of Peak 1 remains following the formation of β$_2$AR-G$_s$$^{EMPTY}$, consistent with a minor population of uncoupled β$_2$AR (Fig. 3*A*).

***TM5, 6, and 7.*** While we observe spectral changes in K227$^{5.56}$, K267$^{6.29}$, K273$^{6.35}$, and R328K$^{7.55}$ upon agonist binding, further changes are observed following G protein coupling (Fig. 4 *A–D*), consistent with changes observed in TM5, TM6, and TM7 in the β$_2$AR-G$_s$ structure (Fig. 4 *E* and *F*). The slight broadening of the peak representing K227$^{5.56}$ upon agonist binding suggests the appearance of two or more conformations in intermediate exchange at the intracellular side of TM5 (Fig. 4*A*). Upon coupling to G$_s$ we see the appearance of a new downfield peak (Peak 2) and a weaker Peak 1 (Fig. 4*A*).

The two TM6 probes, K267$^{6.29}$ and K273$^{6.35}$, show significant differences in terms of peak patterns. In the apo and agonist-bound state K273$^{6.35}$ is represented by two weak peaks, indicating that there are at least two conformations with a slow exchange rate, while K267$^{6.29}$ is represented by a stronger single peak (Fig. 4 *B* and *C*). This is because K267$^{6.29}$ is located at the end of TM6 and its side chain is expected to exhibit relatively high conformational flexibility, whereas K273$^{6.35}$ is located in the transmembrane core and its side chain can interact with neighboring residues I277$^{6.39}$ and R328$^{7.55}$ (Fig. 4 *E* and *F*). Upon agonist binding, there is a downfield shift in the peak representing
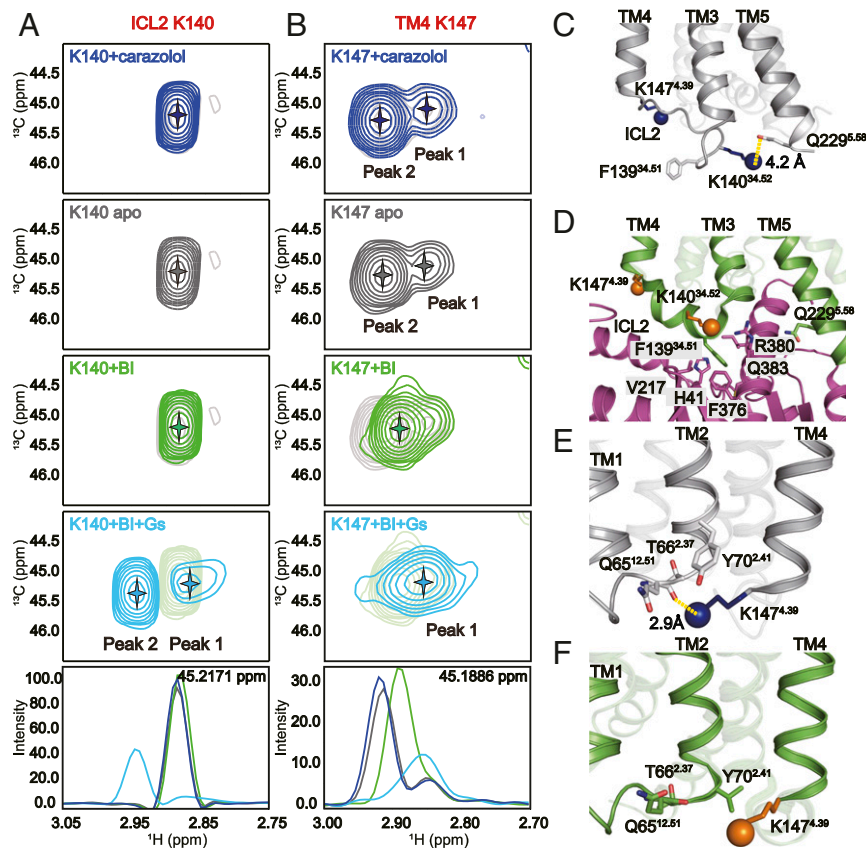
Ma et al.

www.manaraa.com

**Fig. 3.** Conformational changes of ICL2 from inactive to active state. (*A* and *B*) $^1$H-$^{13}$C HSQC spectra of K140$^{34.52}$ (*A*) and K147$^{4.39}$ (*B*). The 1D slices of corresponding $^1$H-$^{13}$C HSQC spectra in H dimension are shown at the bottom. The local environment of the two probes are shown by side views in inactive (gray, *C, E*) and active (green, *D, F*) conformations. G$_{\alpha s}$ is shown in purple (*D*). The agonist BI-167107 is abbreviated by BI.

K267$^{6.29}$. There are two peaks for K267$^{6.29}$ in the β$_2$AR-G$_s$ complex (Fig. 4*B*). Peak 2 has the same chemical shift seen with agonist alone but with marked reduction in intensity. Of note, the dynamics of the cytoplasmic end of TM6 may impact the cytoplasmic end of TM5, given their close proximity (Fig. 4*F*). K227$^{5.56}$ in TM5 is close enough to have a polar interaction with E268$^{6.28}$ (Fig. 4*F*). Thus, the minor Peak 1 in K227$^{5.56}$ and in K267$^{6.29}$ may reflect different TM5–TM6 interactions in a small population of nucleotide-free β$_2$AR-G$_s$ complex.

It is interesting to note that the spectra of K273$^{6.35}$ and R328K$^{7.55}$ are similar (Fig. 4 *C* and *D*). This may be due to the close proximity of K273$^{6.35}$ and R328$^{7.55}$ observed in the inactive state crystal structures (Figs. 1 *C* and *D* and 4*E*) where R328K$^{7.55}$ could form a hydrogen bond with the backbone carbonyl of K270$^{6.32}$. This interaction would be lost upon coupling with G$_s$. For both K273$^{6.35}$ and R328K$^{7.55}$, agonist binding leads to a downfield shift in Peak 1, and Peak 1 is lost in the β$_2$AR-G$_s$ complex. Peak 2 may represent a conformation that is more exposed to the solvent, therefore Peak 2 is less affected by agonist-binding or G protein coupling than Peak 1.

**Conformational Differences in G$_s$ and G$_{i1}$ Coupling.** Recently, a number of GPCR-G$_{i/o}$ complex structures have been determined by cryo-EM (5–7, 25–28). The G$_s$ and β$_2$AR interaction interface is composed by TM3, TM5, TM6, and ICL2. While G$_{\alpha i/o}$ interactions with TM3, TM5, and TM6 are similar in GPCR-G$_{i/o}$ protein complexes, TM2, TM7, and H8 are also involved in formation of the A1 adenosine receptor (A1R)-G$_i$ complex, and ICL2 and the junction between TM7 and H8 contribute to formation of the rhodopsin-G$_i$ complex (*SI Appendix*, Fig. S5). For GPCR-G$_{i/o}$ complexes, the outward displacement of TM6 is

smaller than observed for the β$_2$AR-G$_s$ complex. The differences in the interaction interface for these complexes might contribute to G protein coupling preferences. As noted above, the β$_2$AR can couple to both G$_s$ and G$_i$. However, efforts toward obtaining the structure of β$_2$AR-G$_i$ complex have failed due to the relatively weak interaction and instability of the complex. As a consequence, little is known about differences in the interactions between β$_2$AR and G$_i$ compared with the β$_2$AR-G$_s$ complex.

To provide more structural insights into the basis of β$_2$AR coupling selectivity for G$_s$ over G$_i$, we next sought to compare β$_2$AR binding with G$_s$ and G$_i$ by using the $^1$H-$^{13}$C HSQC spectra of the β$_2$AR-BI-167017-G$_{i1}$$^{EMPTY}$ complex (Fig. 5). The β$_2$AR-G$_{i1}$$^{EMPTY}$ complex was formed by adding the nucleotidase apyrase after complex formation to degrade any released GDP. Fig. 5 compares the spectra of β$_2$AR-G$_s$$^{EMPTY}$ and β$_2$AR-G$_{i1}$$^{EMPTY}$ complexes. Consistent with the previous observation that the β$_2$AR-G$_{i1}$ complex is less stable than the β$_2$AR-G$_s$ complex (29), we observed smaller spectral changes in the β$_2$AR-G$_{i1}$ complex sample. The NMR spectral changes of K227$^{5.56}$, K267$^{6.29}$, K273$^{6.35}$, and R328K$^{7.55}$ corresponding to the conformational changes of TM5, 6, and 7 are similar to those obtained from the β$_2$AR-G$_s$ complex; however, peak 2 of K227$^{5.56}$ and K273$^{6.35}$ and peak 1 of K267$^{6.29}$ are notably weaker in the β$_2$AR-G$_{i1}$ complex compared to the β$_2$AR-G$_s$ complex. However, it's hard to discriminate whether the TM6 outward displacement of β2AR−G$_{i1}$ is smaller than that of β2AR−G$_s$ based on the signal intensity difference observed by NMR.

Remarkably, there are nearly no chemical shift changes for K140$^{34.52}$ in ICL2 and K147$^{4.39}$ in TM4 in the β$_2$AR-G$_{i1}$ complex, which is in contrast to what is observed for β$_2$AR-G$_s$ complex (Fig. 5 *B* and *C*). The observed decrease of peak intensity is likely
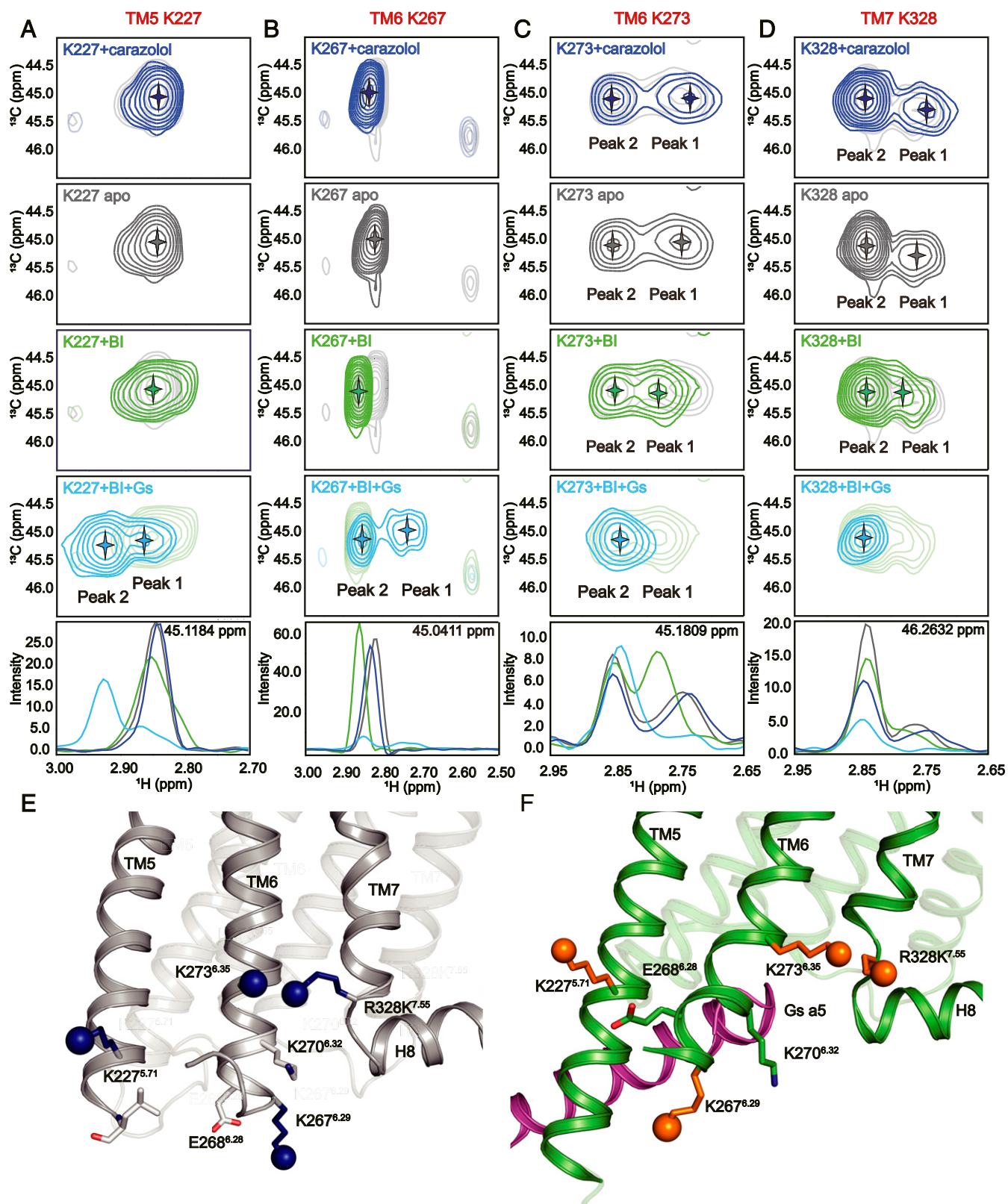
Ma et al.

www.manaraa.com

**Fig. 4.** Conformational changes of TM5, TM6, and TM7 during $\beta_2$AR activation. (*A–D*) The $^1$H-$^{13}$C HSQC spectra of K227$^{5.71}$ (*A*), K267$^{6.29}$ (*B*), K273$^{6.35}$ (*C*), and K328$^{7.55}$ (*D*). The 1D slices of corresponding $^1$H-$^{13}$C HSQC spectra in H dimension are shown at the bottom. The local environments of the four probes are shown in inactive (gray, *E*) and active (green, *F*) conformations. The $\alpha$5 helix from Gs$\alpha$ is shown as purple cartoon. The agonist BI-167107 is abbreviated by BI.
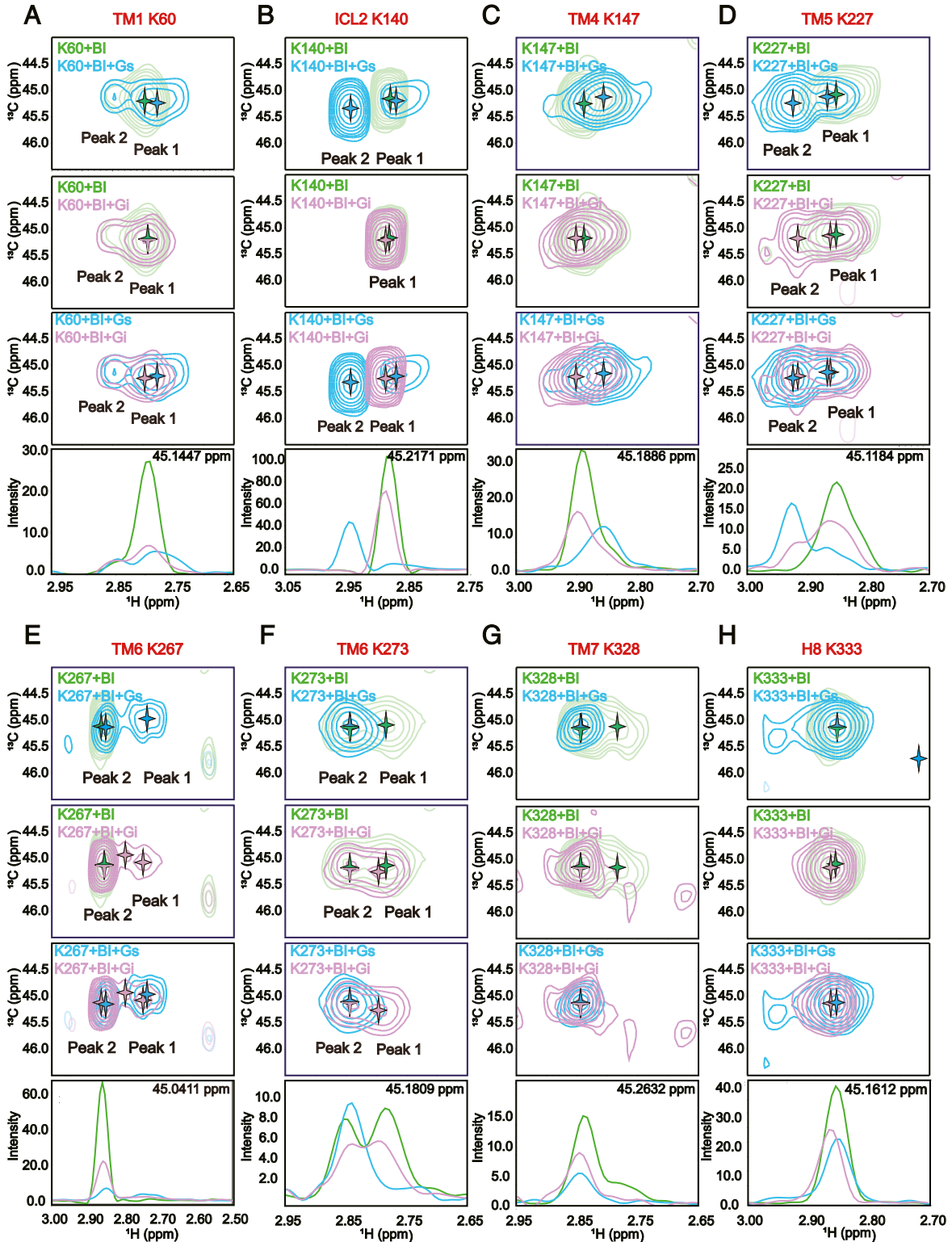
Ma et al.

www.manaraa.com

**Fig. 5.** Comparison of conformational changes in $\beta_2$AR coupled to Gs or Gi1. BI is short for BI-167107. (*A*–*H*) The $^1$H-$^{13}$C HSQC spectra of the eight probes from TM1 to H8. The eight probes are K60$^{1.59}$ (*A*), K140$^{34.52}$ (*B*), K147$^{4.39}$ (*C*), K227$^{5.56}$ (*D*), K267$^{6.29}$ (*E*), K273$^{6.35}$ (*F*), R328K$^{7.55}$ (*G*), and R333K$^{8.51}$ (*H*). For each probe, the overlay of the $^1$H-$^{13}$C HSQC spectra of agonist-bound $\beta_2$AR (green) and $\beta_2$AR-Gs$^{EMPTY}$ (blue) are shown at the top, followed by the comparison of the $^1$H-$^{13}$C HSQC spectra of agonist-bound $\beta_2$AR (green) and $\beta_2$AR-Gi1$^{EMPTY}$ (pink), then by the overlay of $\beta_2$AR-Gs$^{EMPTY}$ (blue) and $\beta_2$AR-Gi1$^{EMPTY}$ (pink). The 1D slices of corresponding $^1$H-$^{13}$C HSQC spectra in H dimension are shown at the bottom.

Ma et al.

www.manaraa.com

due to the increase in mass. The lack of spectral changes for K140[34.52] and K147[4.39] suggest that ICL2 does not form an alpha helix when coupled to $G_{i1}$ and may have only weak interactions with $G_{i1}$, possibly explaining the less efficient coupling and the overall instability of the $\beta_2AR$-$G_{i1}$ complex.

As noted above, the insertion of F139[34.51] in ICL2 of the $\beta_2AR$ into a hydrophobic pocket formed by H41, V217, F376, C379, and R380 in the $G_{\alpha s}$ is essential for GDP release (*SI Appendix*, Figs. S6*A* and S7*A*). Of these, only F376 is conserved as F336 in $G_i$ (*SI Appendix*, Fig. S6 *B* and *C*). When comparing sequences of ICL2 from GPCRs that couple to $G_s$, $G_{i/o}$, $G_{q/11}$, and $G_{12}$, position 34.51 is most often a L, F, I, or M for $G_s$ coupled receptors, while a broader range of amino acids are found in $G_{i/o}$ coupled

receptors (*SI Appendix*, Fig. S6*D*). It is possible that interactions with 34.51 in ICL2 may be less important for coupling with $G_{i1}$ than with $G_s$. This is in agreement with the recent structures of $G_i$ in complex with the cannabinoid receptor subtype 1 (CB1) (27), the μ-opioid receptor (μOR) (6), and the A1R (7). For these receptors, the interactions between the amino acid at position 34.51 in ICL2 (L in CB1 and A1R, and V in μOR) and $G_i$ are much weaker, interacting with only one or two side chains of $G_i$ (*SI Appendix*, Fig. S7 *B–D*). However, this weaker interaction between ICL2 and $G_i$ is not universal. For the neurotensin receptor subtype 1 (NTSR1), which couples promiscuously to $G_{i/o}$, $G_s$, and $G_{q/11}$ (30), F174[34.51] in ICL2 packs into a pocket formed by four amino acids in $G_i$ (*SI Appendix*, Fig. S7*E*). The importance of the amino
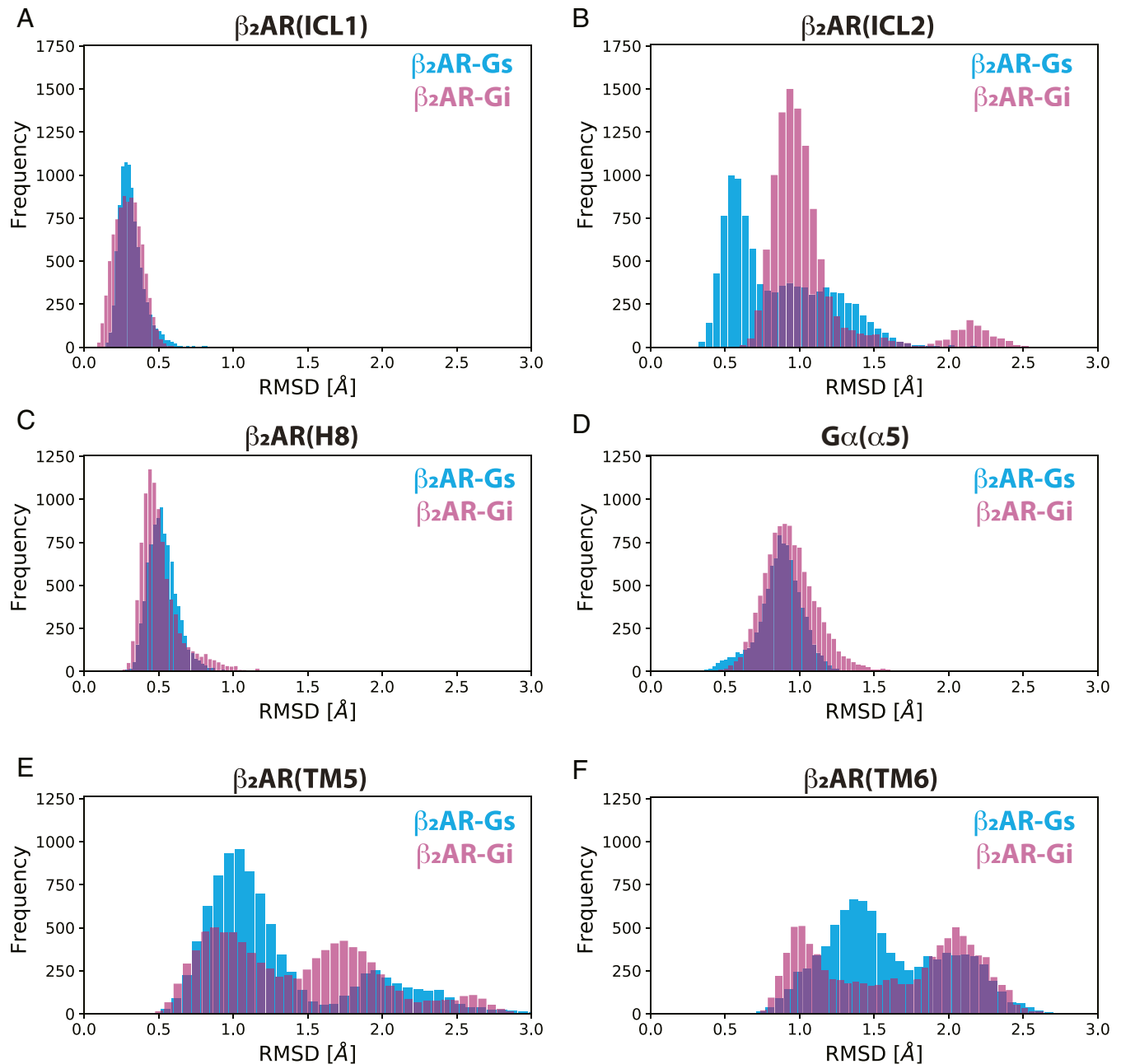
**Fig. 6.** Comparison of conformational changes measured by MD simulations in $\beta_2AR$ coupled to $G_s$ or $G_i$. Backbone rmsd in Å extracted from $3 \times 3$-μs-long MD simulations of $\beta_2AR$-Gi (pink) and $\beta_2AR$-Gs (cyan) of structural elements at the receptor-G protein interface. (*A*) ICL1 of $\beta_2AR$: E62[12.48]-Q65[12.51]. (*B*) ICL2 of $\beta_2AR$: I135[3.54]-A150[4.42]. (*C*) H8 of $\beta_2AR$: S329[8.47]-C341[8.59]. (*D*) α5 helix of Gαi and Gαs. (*E*) TM5 of $\beta_2AR$: N196[5.35]-R239[ICL3]. (*F*) TM6 of $\beta_2AR$: C265[6.27]-Q299[6.61]. The rmsd values were calculated relative to the respective structural element in the starting structure of $\beta_2AR$-Gi[EMPTY] and $\beta_2AR$-Gs[EMPTY].

Ma et al.

acid in position 34.51 was initially demonstrated for the $G_{q/11}$ coupled M1 muscarinic receptor (M1R) where the substitution of $L131^{34.51}$ for Ala in ICL2 led to a loss of $G_{q/11}$ coupling (24). In the recent cryo-EM structure of the M1R-G11 complex, $L131^{34.51}$ packs into a pocket formed by four amino acids in G11 (28) (*SI Appendix*, Fig. S7F). Like $G_s$ coupled GPCRs, L, F, I, or M are more commonly found at position 34.51 in $G_{q/11}$ coupled GPCRs (*SI Appendix*, Fig. S6D). While the evidence suggests that weak interactions between $F139^{34.51}$ in ICL2 of the $\beta_2AR$ and $G_{i1}$ may account for poor coupling efficiency, we cannot exclude the possibility that $\beta 2AR$ simply couples less efficiently to $G_i$ and the lack of strong engagement with ICL2 is a manifestation of that.

Similar to $G_s$, $G_{i1}$ binding also has little effect on $R333K^{8.51}$ located at H8 (Fig. 5H). The decrease in intensity is likely due to the increased size of the complex. Notably, the decrease in intensity is greater for $G_s^{EMPTY}$ compared to $G_{i1}^{EMPTY}$, consistent with the formation of a more stable complex. The low intensity downfield peak observed in $R333K^{8.51}$ with $G_s$ is not observed with $G_{i1}$. The spectra of $K60^{1.59}$ in TM1 are similar for $G_s$ and $G_{i1}$, with a reduction of intensity and the peak splitting into a slightly upfield-shifted peak and a smaller downfield peak (Fig. 5A). ICL1 and H8 are not observed to interact with Gs in the $\beta_2AR$-$G_s$ complex; however, the orientation of ICL1 relative to H8 changes upon complex formation with the loss of an electrostatic interaction between $K60^{1.59}$ in ICL1 and $R328K^{7.55}$ in H8.

We have previously observed evidence for a transient intermediate state following the disruption of the $\beta_2AR$-$G_s$ complex by the addition of GDP (8). In an effort to detect this state by NMR spectroscopy, we formed $\beta_2AR$-$G_s$ and $\beta_2AR$-$G_{i1}$ complexes in the presence of 300 μM GDP. As can be seen in *SI Appendix*, Figs. S8 and S9, we don't observe a distinct state in the presence of GDP. The spectra are consistent with a mixture of nucleotide-free $\beta_2AR$-$G_s$ or $\beta_2AR$-$G_{i1}$, and $\beta_2AR$ bound to agonist alone. Our inability to detect a distinct GDP-bound $\beta_2AR$-Gs complex could be due to the insensitivity of our probes or to the fact that the amount of the intermediate may be too small to detect.

**Molecular Dynamics Simulations Showed Different ICL2 Behavior in the $\beta_2AR$-$Gi^{EMPTY}$ and the $\beta_2AR$-$Gs^{EMPTY}$ Complex.** To investigate the dynamics at the receptor G protein interface, classical unbiased MD simulations of the $\beta_2AR$-$G_{i1}^{EMPTY}$ and the $\beta_2AR$-$G_s^{EMPTY}$ complex were carried out. The $\beta_2AR$-$G_{i1}^{EMPTY}$ model was built based on the $\beta_2AR$-$G_s^{EMPTY}$ complex (Protein Data Bank [PDB] ID code: 3SN6) (see *Methods* for more details) and as a result, ICL2 in the starting structures of both $\beta_2AR$-$G_{i1}^{EMPTY}$ and $\beta_2AR$-$G_s^{EMPTY}$ complex are in an alpha-helical conformation. Three independent, 3-μs-long molecular dynamics (MD) simulations were carried. While the simulations are too short to observe unfolding of the secondary structure, the significantly higher rmsd of the ICL2 region of the $\beta_2AR$-$G_{i1}$ complex compared to the $\beta_2AR$-$G_s$ complex suggests the starting alpha-helical structure of ICL2 is less stable in the $\beta_2AR$-$G_{i1}^{EMPTY}$ structure. Of note, such changes are not observed for ICL1, H8, nor $G_\alpha(\alpha5)$ when both systems are compared (Fig. 6 A–D). The only other structural elements at the receptor G protein interface with increased rmsd values are TM5 and TM6 (Fig. 6 E and F),

consistent with the high dynamics of their cytoplasmic ends observed by chemical shift analysis in $\beta_2AR$-$G_{i1}^{EMPTY}$ and in $\beta_2AR$-$G_s^{EMPTY}$ complexes. A close inspection of the MD simulations results suggests a higher flexibility of $K140^{34.52}$ and $K147^{4.39}$ from ICL2 for the $\beta_2AR$-$G_{i1}^{EMPTY}$ compared to ICL2 from $\beta_2AR$-$G_s^{EMPTY}$ as measured by the average rms fluctuation (RMSF) (*SI Appendix*, Fig. S10). The average RMSF value for $K140^{34.52}$ is two times higher and for $K147^{4.39}$ is six times higher in $\beta_2AR$-$G_{i1}^{EMPTY}$ than $\beta_2AR$-$G_s^{EMPTY}$. The MD simulations results are in agreement with the NMR experimental observation that ICL2 plays different roles when $\beta_2AR$ couples to $G_i$ or $G_s$.

## Discussion

We applied NMR spectroscopy to monitor structural changes in the cytoplasmic surface of the unliganded $\beta_2AR$ and in response to an inverse agonist, an agonist, $G_s$, and $G_i$. We have been unable to obtain crystal or cryo-EM structures of the apo-$\beta_2AR$ and agonist-bound $\beta_2AR$ due to its instability and possibly due to conformational heterogeneity. Our NMR studies provide further evidence for conformational heterogeneity as we observe more than one peak for $K147^{4.39}$, $K273^{6.35}$, and $K328^{7.55}$ in apo and agonist-bound $\beta_2AR$ (Figs. 2–4). Agonist binding leads to changes in $K147^{4.39}$ in ICL2, $K267^{6.29}$, and $K273^{6.35}$ in TM6, and in $K328^{7.55}$ in TM7; however, additional changes are observed upon the addition of $G_s$ and $G_{i1}$. This suggests that for the $\beta_2AR$ agonist, binding alone cannot fully stabilize the G protein bound conformation, as has been observed in previous fluorescence and double electron electron resonance spectroscopy experiments (8, 13). The structural changes stabilized by $G_{i1}$ and $G_s$ are qualitatively the same for TM5, TM6, and TM7; however, our NMR studies and supporting MD simulations suggest that $G_{i1}$ does not promote the formation of an alpha helix in ICL2.

## Methods

The receptors were expressed in *Sf*9 insect cells, purified by affinity column and size exclusion chromatography, and labeled by reductive methylation. NMR data were collected at 25 °C on a Burker Avance 800-MHz spectrometer equipped with a cryoprobe. The $^1H$-$^{13}C$ HSQC spectra were recorded with spectral width of 11,160.71428 Hz in the $^1H$-dimension (w1) and 14,492.7536 Hz in the $^{13}C$-dimension (w2) centered at 46 ppm. For all spectra, 1024 × 256 complex points were recorded and a relaxation delay of 2 s was used to allow spin to relax back to equilibrium. MD simulations were performed using Gromacs simulation package. Further details are proved in *SI Appendix*.

**Data Availability.** All study data are included in the article and *SI Appendix*.

1. D. Hilger, M. Masureel, B. K. Kobilka, Structure and dynamics of GPCR signaling complexes. *Nat. Struct. Mol. Biol.* **25**, 4–12 (2018).
2. A. Manglik, B. Kobilka, The role of protein dynamics in GPCR function: Insights from the β2AR and rhodopsin. *Curr. Opin. Cell Biol.* **27**, 136–143 (2014).
3. R. P. Xiao, Beta-adrenergic signaling in the heart: Dual coupling of the beta2-adrenergic receptor to G(s) and G(i) proteins. *Sci. STKE* **2001**, re15 (2001).
4. S. G. Rasmussen *et al.*, Crystal structure of the β2 adrenergic receptor-Gs protein complex. *Nature* **477**, 549–555 (2011).
5. Y. Kang *et al.*, Cryo-EM structure of human rhodopsin bound to an inhibitory G protein. *Nature* **558**, 553–558 (2018).

6. A. Koehl *et al.*, Structure of the μ-opioid receptor-G_i protein complex. *Nature* **558**, 547–552 (2018).
7. C. J. Draper-Joyce *et al.*, Structure of the adenosine-bound human adenosine A(1) receptor-G(i) complex. *Nature* **558**, 559–563 (2018).
8. G. G. Gregorio *et al.*, Single-molecule analysis of ligand efficacy in β₂AR-G-protein activation. *Nature* **547**, 68–73 (2017).
9. Y. Du *et al.*, Assembly of a GPCR-G protein complex. *Cell* **177**, 1232–1242.e11 (2019).
10. M. Casiraghi, J.-L. Banères, L. J. Catoire, "NMR Spectroscopy for the Characterization of GPCR Energy Landscapes" in *Structure and Function of GPCRs*, G. Lebon, Ed. (Springer International Publishing, 2019), pp. 27–52.

www.manaraa.com

11. M. P. Bokoch *et al*., Ligand-specific regulation of the extracellular surface of a G-protein-coupled receptor. *Nature* **463**, 108–112 (2010).

12. R. Nygaard *et al*., The dynamic process of β(2)-adrenergic receptor activation. *Cell* **152**, 532–542 (2013).

13. A. Manglik *et al*., Structural insights into the dynamic process of β2-Adrenergic receptor signaling. *Cell* **161**, 1101–1111 (2015).

14. R. Sounier *et al*., Propagation of conformational changes during μ-opioid receptor activation. *Nature* **524**, 375–378 (2015).

15. J. Xu *et al*., Conformational complexity and dynamics in a muscarinic receptor revealed by NMR spectroscopy. *Mol. Cell* **75**, 53–65.e7 (2019).

16. L. Ye *et al*., Mechanistic insights into allosteric regulation of the $A_{2A}$ adenosine G protein-coupled receptor by physiological cations. *Nat. Commun.* **9**, 1372 (2018).

17. A. B. Kleist *et al*., "Site-specific side chain labeling for NMR studies of G protein-coupled receptors" in *Methods in Cell Biology*, A. K. Shukla, Ed. (Academic Press, 2019), Vol. 149, pp. 259–288.

18. S. T. Larda, M. P. Bokoch, F. Evanics, R. S. Prosser, Lysine methylation strategies for characterizing protein conformations by NMR. *J. Biomol. NMR* **54**, 199–209 (2012).

19. A. L. Parola, S. Lin, B. K. Kobilka, Site-specific fluorescence labeling of the beta2 adrenergic receptor amino terminus. *Anal. Biochem.* **254**, 88–95 (1997).

20. K. Xiao, S. K. Shenoy, Beta2-adrenergic receptor lysosomal trafficking is regulated by ubiquitination of lysyl residues in two distinct receptor domains. *J. Biol. Chem.* **286**, 12785–12795 (2011).

21. J. A. Ballesteros, H. Weinstein, "Integrated methods for the construction of three-dimensional models and computational probing of structure-function relations in G protein-coupled receptors" in *Methods in Neurosciences*, S. C. Sealfon, Ed. (Academic Press, 1995), Vol. 25, pp. 366–428.

22. D. M. Rosenbaum *et al*., GPCR engineering yields high-resolution structural insights into beta2-adrenergic receptor function. *Science* **318**, 1266–1273 (2007).

23. X. Liu *et al*., Mechanism of β$_2$AR regulation by an intracellular positive allosteric modulator. *Science* **364**, 1283–1287 (2019).

24. O. Moro, J. Lameh, P. Högger, W. Sadée, Hydrophobic amino acid in the i2 loop plays a key role in receptor-G protein coupling. *J. Biol. Chem.* **268**, 22273–22276 (1993).

25. J. García-Nafría, Y. Lee, X. Bai, B. Carpenter, C. G. Tate, Cryo-EM structure of the adenosine $A_{2A}$ receptor coupled to an engineered heterotrimeric G protein. *eLife* **7**, e35946 (2018).

26. J. García-Nafría, R. Nehmé, P. C. Edwards, C. G. Tate, Cryo-EM structure of the serotonin 5-HT$_{1B}$ receptor coupled to heterotrimeric G$_o$. *Nature* **558**, 620–623 (2018).

27. K. K. Kumar *et al*., Structure of a signaling cannabinoid receptor 1-G protein complex. *Cell* **176**, 448–458.e12 (2019).

28. S. Maeda, Q. Qu, M. J. Robertson, G. Skiniotis, B. K. Kobilka, Structures of the M1 and M2 muscarinic acetylcholine receptor/G-protein complexes. *Science* **364**, 552–557 (2019).

29. M. J. Strohman *et al*., Local membrane charge regulates β$_2$ adrenergic receptor coupling to G$_{i3}$. *Nat. Commun.* **10**, 2234 (2019).

30. É. Besserer-Offroy *et al*., The signaling signature of the neurotensin type 1 receptor with endogenous ligands. *Eur. J. Pharmacol.* **805**, 1–13 (2017).

**PHARMACOLOGY**

Ma et al.